ADVANCED MATERIALS
www.advmat.de

Colossal Electromechanical Response in Antiferroelectric-based Nanoscale Multilayers

*Megha Acharya, Louis Alaerts, Ella Banyas, Deokyoung Kang, Francesco Ricci, Hao Pan, Brendan Hanrahan, Jonathan E. Spanier, Jeffery B. Neaton, Geoffroy Hautier, and Lane W. Martin**

The pursuit of smaller, energy-efficient devices drives the exploration of electromechanically active thin films (<1 µm) to enable micro- and nano-electromechanical systems. While the electromechanical response of such films is limited by substrate-induced mechanical clamping, large electromechanical responses in antiferroelectric and multilayer thin-film heterostructures have garnered interest. Here, multilayer thin-film heterostructures based on antiferroelectric $PbHfO_3$ and ferroelectric $PbHf_{1-x}Ti_xO_3$ overcome substrate clamping to produce electromechanical strains >4.5%. By varying the chemistry of the $PbHf_{1-x}Ti_xO_3$ layer (x = 0.3-0.6) it is possible to alter the threshold field for the antiferroelectric-to-ferroelectric phase transition, reducing the field required to induce the onset of large electromechanical response. Furthermore, varying the interface density (from 0.008 to 3.1 nm^{-1}) enhances the electrical-breakdown field by >450%. Attaining the electromechanical strains does not necessitate creating a new material with unprecedented piezoelectric coefficients, but developing heterostructures capable of withstanding large fields, thus addressing traditional limitations of thin-film piezoelectrics.

1. Introduction

Building from extensive work on piezoelectric-based micro- (MEMS) and nano-electromechanical (NEMS) systems,[1–5] researchers are exploring using piezoelectrics to enable new devices such as low-power piezoelectric transistors (where a piezoelectric element drives a metal-to-insulator transition in a piezoresistive element)[6–8] and piezoelectric-based logic-in-memory devices [e.g., derived from versions of the magnetoelectric spin-orbit (MESO) device wherein magnetic spins are controlled using electric field via strain-induced coupling from piezoelectrics].[6–8] In bulk-ceramic and single-crystal forms, the morphotropic phase boundary-based (MPB) compositions of $PbZr_{0.52}Ti_{0.48}O_3$[9,10] and $0.68PbMg_{1/3}Nb_{2/3}O_3$-$0.32PbTiO_3$[11] have been lauded for their superior piezoelectric strains. In thin films (<1 µm thick),

M. Acharya, D. Kang, H. Pan, L. W. Martin
Department of Materials Science and Engineering
University of California
Berkeley, CA 94720, USA
E-mail: lwmartin@rice.edu

M. Acharya, E. Banyas, F. Ricci, J. B. Neaton, L. W. Martin
Materials Sciences Division
Lawrence Berkeley National Laboratory
Berkeley, CA 94720, USA

L. Alaerts, G. Hautier
Thayer School of Engineering
Dartmouth College
Hanover, NH 03755, USA

E. Banyas, J. B. Neaton
Department of Physics
University of California
Berkeley, CA 94720, USA

B. Hanrahan
DEVCOM U.S. Army Research Laboratory
Adelphi, MD 20783, USA

J. E. Spanier
Department of Mechanical Engineering and Mechanics
Drexel University
Philadelphia, PA 19104, USA

J. B. Neaton
Molecular Foundry
Lawrence Berkeley National Laboratory
Berkeley, CA 94720, USA

J. B. Neaton
Kavli Energy Nanosciences Institute
University of California
Berkeley, CA 94720, USA

L. W. Martin
Departments of Materials Science and Nanoengineering
Chemistry
and Physics and Astronomy
Rice University
Houston, TX 77005, USA

L. W. Martin
Rice Advanced Materials Institute
Rice University
Houston, TX 77005, USA

The ORCID identification number(s) for the author(s) of this article can be found under https://doi.org/10.1002/adma.202419690

DOI: 10.1002/adma.202419690

however, such materials exhibit responses that are just 10–50% of bulk versions[12] in large part due to substrate-induced lateral clamping[1,3,5] of the film which results in reduced extrinsic (domain-wall) contributions and elastic limits on the change of shape of the material.[13–17] This has led to complex strategies to overcome these limitations including extensive work on nanostructuring films to reduce in-plane clamping effects;[6,16–18] an approach that culminated in researchers creating antiphase boundaries between nanopillar-like structures to realize electromechanical strain (ε) ≈ 1.4% at 1 kHz.[19,20] While interesting, such approaches are not always compatible with the desired device geometries. Other promising approaches include the exploration of less-studied classes of materials, including antiferroelectrics such as $PbZrO_3$ which has shown the potential to realize large ϵ (≈ 1–1.1%)[21,22] in thin films (down to ≈100-300 nm in thickness). The electromechanical response of antiferroelectrics arises primarily from a field-driven antiferroelectric-to-ferroelectric phase transition and the corresponding change in lattice parameters and unit-cell volume. In a recent work, the electromechanical response of single-layer $PbZrO_3$ heterostructures was found to be enhanced due to the coupling between the antiferroelectric-to-ferroelectric phase transition and the substrate-induced constraints at the "unit-cell level" causing the associated volume expansion to be directed in the out-of-plane direction as seen in the measured electromechanical response.[22] At the same time, there have been intriguing observations of large ε (≈ 1%) in thin-film multilayers of non-polar binary oxides largely thought to arise form electrostriction.[23–25] Such results raise the question of the true limits of electromechanical response in thin-film materials while hinting at pathways to achieve larger effects.

Here, by producing antiferroelectric-based nanoscale multilayers one can take advantage of the antiferroelectric-to-ferroelectric phase transition, piezoelectric responses, and electrostrictive contributions enabled by increased electrical breakdown fields (E_B) to achieve colossal electromechanical strains. This work explores multilayers based on the $PbHf_{1-x}Ti_xO_3$ system where the end member $PbHfO_3$ is a robust antiferroelectric[26] and $0.3 \leq x \leq 0.6$ versions are ferroelectric and near the MPB.[27] Prior to studying the multilayers, single-layer films with x = 0, 0.3, 0.4, 0.5, and 0.6 were synthesized (Experimental Section). X-ray diffraction studies (Experimental Section) and electromechanical measurements (Experimental Section) for single-layer $PbHfO_3$ (Figure S1, Supporting Information) and various $PbHf_{1-x}Ti_xO_3$ (Figures S2 and S3; Note S1, Supporting Information) films reveal that all materials have similar robust electromechanical and structural response akin to well-studied antiferroelectric[21,22] (ε = 1.1%) and MPB-based[12,27] (ε = 0.4-0.6%) thin-film materials. In terms of the nature of the response, antiferroelectrics (e.g., $PbHfO_3$) are expected to undergo an antiferroelectric (non-polar, orthorhombic) to ferroelectric (polar, rhombohedral) phase transition upon applying a threshold electric field (E_T) with a noticeable change in slope between two linear regimes in the strain-electric field plot (Figure S1c, Supporting Information).[22,28–31] For ferroelectrics (e.g., $PbHf_{1-x}Ti_xO_3$, x = 0.3-0.6), however, ε increases (approximately) linearly with field.[12,27] Having noted the differences in electromechanical response between the two classes of materials under study, efforts transitioned to exploring nanoscale multilayers built from the same.

2. Results and Discussion

120-nm-thick multilayer heterostructures based on the antiferroelectric $PbHfO_3$ and ferroelectric $PbHf_{1-x}Ti_xO_3$ (x = 0.3, 0.4, 0.5, and 0.6) with interface densities ranging from 0.008 to 3.1 nm^{-1} [corresponding to layers that were 60 nm (a bilayer with one interface) to 0.32 nm (a multilayer with 372 interfaces) thick] were synthesized on $SrTiO_3$ (001) substrates with $SrRuO_3$ as the top and bottom electrodes (Experimental Section). Henceforth, heterostructure variants will be referred to in the form $PbHfO_3/PbHf_{1-x}Ti_xO_3$ (n nm^{-1}) where n is the interface density.[32,33] For example, regardless of chemistry (x = 0.3, 0.4, 0.5, and 0.6), $PbHfO_3/PbHf_{1-x}Ti_xO_3$ (1.5 nm^{-1}) heterostructures (with layers that are 0.67 nm thick) were found to be single-crystalline with periodic interfaces between the constituent layers in the out-of-plane direction as indicated by the presence of multiple satellite peaks in X-ray line (**Figure 1a**) and RSM (Figure S4, Supporting Information) scans. While ε for the $PbHfO_3$ and $PbHf_{1-x}Ti_xO_3$ single-layer heterostructures was in the range 0.4-1.1% (Figures S1 and S2, Supporting Information),[27] all the resulting multilayer heterostructures exhibited strain-electric field responses of the same form as those observed in single-layer antiferroelectrics but with considerably higher values (3–4.8%), depending on the chemistry of the $PbHf_{1-x}Ti_xO_3$ layer (Figure 1b). The observed ε values surpass prior reports on both thin-film heterostructures and bulk versions for (anti)ferroelectric-, relaxor-, and oxide-based systems (Figure 1c; Table S1, Supporting Information). Furthermore, multilayer-based heterostructures (again using those with an interface density of 1.5 nm^{-1} as an example) also exhibit dramatically enhanced E_B (>6.8 MV cm^{-1}); significantly higher than for single-layer $PbHfO_3$ (1.23 MV cm^{-1})[26] and $PbHf_{1-x}Ti_xO_3$ (0.75 MV cm^{-1})[27] films. The result is 0.7% strain at just 100 kV cm^{-1} (1.2 V), 1.9% strain at 1000 kV cm^{-1} (12 V), and the remarkable ability to apply fields as large as 10 MV cm^{-1} (120 V) thereby producing colossal $\varepsilon \approx 4.8\%$. For context, the maximum ε reported in other polar, complex-oxide material systems (both thin-film and bulk versions) is <2.5% (Figure 1c), including that for parent $PbHf_{1-x}Ti_xO_3$ compositions. What is extraordinary, is that the heterostructures do not have effective piezoelectric coefficients that are record breaking, but still give rise to large overall responses. For example, one can consider three effective converse piezoelectric coefficients (d^*_{ij}) for the system: 1) an overall response (based on a linear fit to the entire dataset) which results in values ≈30–55 pm V^{-1}, 2) a low-field response that encompasses the sharp step in response which results in values ≈170.5 pm V^{-1}, and 3) a high-field response that encompasses the data after the sharp step which results in values ≈30–35 pm V^{-1}. In all cases, the values are consistent with values measured in thin-film systems; the ability to apply such large fields, thus producing such large electromechanical responses, are not. These observations highlight the potential of antiferroelectric-based multilayer heterostructures as consequential candidates for superior electromechanical response.

2.1. Varying Chemistry in the Nanoscale-Multilayer Heterostructures

To better understand the evolution of the colossal ε, the chemistry (and, consequentially, the structure) and the periodicity of

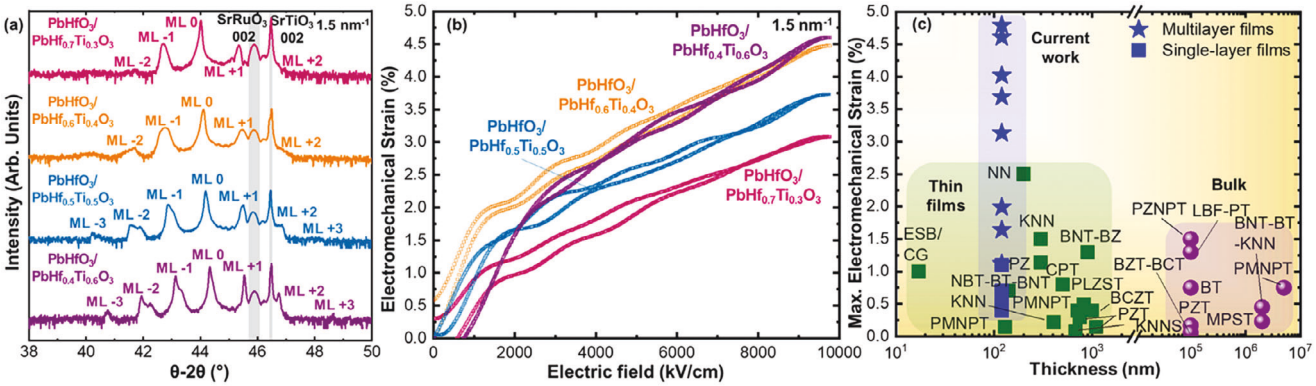

Figure 1. a) X-ray-diffraction measurements (θ-2θ line scan) and b) electromechanical strain (%) extracted from the surface displacement loops as a function of electric field (positive bias) at a frequency of 1 kHz for 120-nm-thick $PbHfO_3/PbHf_{0.7}Ti_{0.3}O_3$, $PbHfO_3/PbHf_{0.6}Ti_{0.4}O_3$, $PbHfO_3/PbHf_{0.5}Ti_{0.5}O_3$, and $PbHfO_3/PbHf_{0.4}Ti_{0.6}O_3$ heterostructures, all with an interface density of 1.5 nm^{-1}. c) Summary of the maximum electromechanical strain values observed for anti(ferroelectric), relaxor ferroelectric, and various oxide-based materials reported in the recent past. References are provided in Table S1 (Supporting Information).

the multilayers was explored systematically to see how these variables influence the evolution of the electromechanical response. Starting with chemistry, it was already shown (Figure 1b) that the $PbHfO_3/PbHf_{0.6}Ti_{0.4}O_3$ (1.5 nm^{-1}) heterostructures exhibit the fastest low-field increase and one of the highest overall electromechanical responses. To explain why this happens, it is illustrative to briefly explore the $PbHf_{1-x}Ti_xO_3$ system wherein changing the chemistry results in a series of structural-phase transitions such that the system goes from an orthorhombic (*Pbam*) phase for x = 0[26] to a rhombohedral (*R3c*) phase for x = 0.1-0.3 to a mixed-phase regime [i.e., a mixture of *R3c*, monoclinic (*Cm*), and tetragonal (*P4mm*) phases] in the range of x = 0.4-0.55, before finally transitioning to a purely *P4mm* phase for x = 0.6-1.[32,34] The same is reflected in polarization-electric field hysteresis loops (Figure S5, Supporting Information) where the coercive field and the magnitude of polarization increases with x.[27] In the same spirit, considering the net composition is expected to be hafnium-rich (i.e., between $PbHf_{0.85}Ti_{0.15}O_3$ and $PbHf_{0.70}Ti_{0.30}O_3$) in the various $PbHfO_3/PbHf_{1-x}Ti_xO_3$ (x = 0.3, 0.4, 0.5, 0.6) multilayers, there is an increasing likelihood for a mixed-phase structure rich in the *R3c* phase with decreasing x. This is confirmed by X-ray diffraction-based azimuthal (ϕ) scans (Experimental Section) which reveal that the $PbHf_{1-x}Ti_xO_3$ layers for the $PbHfO_3/PbHf_{1-x}Ti_xO_3$ (1.5 nm^{-1}) (x = 0.3, 0.4, 0.5, 0.6) multilayers are primarily *R3c* (x = 0.3), mixed-phase (i.e., a mixture of *R3c*, *Cm*, and *P4mm* phases; x = 0.4), *Cm* (x = 0.5), and a mixture of *Cm* and *P4mm* (x = 0.6) (**Figure 2a–d**; Note S1, Supporting Information). Thus, the strong low-field increase of the electromechanical response in the $PbHfO_3/PbHf_{0.6}Ti_{0.4}O_3$ (1.5 nm^{-1}) heterostructures arises from the fact that the chemistry induces a mixed-phase structure wherein those phases are nearly energetically degenerate and thus can be readily transformed from one to another by an applied field. This manifests as a lower field for the onset of the phase transition and initial large increase in strain.

This observation is further supported by exploring the electrical response (i.e., polarization- and switching-current-density-electric field response) for the single- and multi-layer heterostructures. To visualize the onset of the field-induced phase transition, primary focus is given to the current-density-electric field response. Antiferroelectric $PbHfO_3$ exhibits a double bipolar hysteresis in the polarization-electric field response (Figure S1b, Supporting Information) and is characterized by the presence of four peaks at the threshold field values for the antiferroelectric-to-ferroelectric structural phase transition under positive (E_{T1}^+, E_{T2}^+) and negative (E_{T1}^-, E_{T2}^-) fields (Figure 2e; Figure S6a, Supporting Information). Ferroelectric $PbHf_{0.6}Ti_{0.4}O_3$, however, only exhibits two peaks ($E_{T1}^+$and E_{T1}^-) due to a single hysteresis (Figure S6b, Supporting Information). Consequently, the $PbHfO_3/PbHf_{1-x}Ti_xO_3$ (1.5 nm^{-1}) heterostructures exhibit an amalgamation of responses from $PbHfO_3$ and $PbHf_{1-x}Ti_xO_3$. For example, in $PbHfO_3/PbHf_{0.4}Ti_{0.6}O_3$ (1.5 nm^{-1}) heterostructures there are four peaks in the current-electric field response (i.e., antiferroelectric-like) but this gradually transitions to two peaks for $PbHfO_3/PbHf_{0.7}Ti_{0.3}O_3$ (1.5 nm^{-1}) heterostructures (i.e., ferroelectric-like) such that the threshold field (E_{T1} and E_{T2}) is controlled by the composition of the $PbHf_{1-x}Ti_xO_3$ layers (Figure 2f; Figure S6c, Supporting Information). Beyond setting the overall composition of the multilayer heterostructures, the tendency of the $PbHfO_3$ layers to undergo a field-induced structural phase transition to the ferroelectric *R3m* phase[33] is likely facilitated by the proximity of the hafnium-rich $PbHf_{1-x}Ti_xO_3$ layers (which are ferroelectric with *R3c* symmetry). This leads to more ferroelectric-like behavior in $PbHfO_3/PbHf_{0.7}Ti_{0.3}O_3$ heterostructures wherein E_{T1} and E_{T2} merge into just E_{T1} akin to that for a ferroelectric with a net composition of $PbHf_{0.85}Ti_{0.15}O_3$. In the same spirit, on the titanium-rich side (i.e., $PbHfO_3/PbHf_{0.4}Ti_{0.6}O_3$ heterostructures), the system behaves primarily antiferroelectric-like with E_{T1} and E_{T2} being distinct.

Such mutual interdependence of composition, symmetry, and functional behavior within the multilayer heterostructures is also instrumental in simultaneously manipulating the polarization-field response (**Figure 3**; Figures S6d–g, Supporting Information). The atypical electrical response of the studied heterostructures could raise the question about the effects of depolarizing fields within the constituent layers. It is important to note that antiferroelectric materials are fundamentally different from

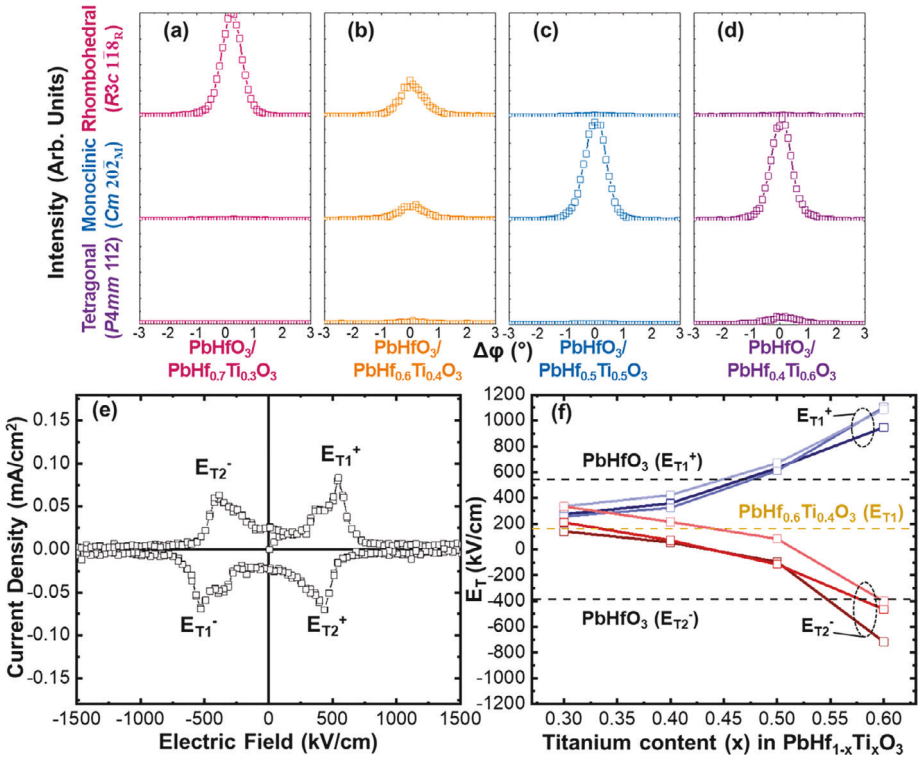

Figure 2. X-ray-diffraction measurements (azimuthal scans) about the *R*3*c* $1\bar{1}8_R$-, *Cm* $20\bar{2}_M$-, and *P*4*mm* 112-diffraction conditions for the $PbHf_{1-x}Ti_xO_3$ system where the subscripts "R" and "M" represent rhombohedral and monoclinic indices, respectively, performed on 120-nm-thick a) $PbHfO_3/PbHf_{0.7}Ti_{0.3}O_3$, b) $PbHfO_3/PbHf_{0.6}Ti_{0.4}O_3$, c) $PbHfO_3/PbHf_{0.5}Ti_{0.5}O_3$, and d) $PbHfO_3/PbHf_{0.4}Ti_{0.6}O_3$ (1.5 nm^{-1}) heterostructures. e) Current density-electric field response for 100-nm-thick $PbHfO_3$ heterostructures. f) The threshold electric field (E_T) for the onset of the antiferroelectric-to-ferroelectric phase transformation for various $PbHfO_3/PbHf_{1-x}Ti_xO_3$ (1.5 nm^{-1}) heterostructures as a function of the composition (x) of the $PbHf_{1-x}Ti_xO_3$ layer.

paraelectric or dielectric materials which possess zero intrinsic polarization. Multiple experimental studies related to antiferroelectric $PbHfO_3$[22,35–38] point toward antipolar displacements of Pb^{+2} ions (akin to that in $PbZrO_3$) as the reason for a net-zero polarization at zero applied bias even as thin films. As such, even if there is an influence of depolarizing field at the interfaces of the ferroelectric/antiferroelectric layers, it is less likely to be observed in the measured response as the antipolar displacement of the Pb^{+2} ions would still result in a net-zero polarization at zero applied bias in all cases. Additionally, the dependence of the E_T values on the chemistry of the multilayers would not be observed (Figure 2f). This would be primarily because the effect of depolarizing field is strongly dependent on the thickness of the ferroelectric material in the thin-film heterostructures. Considering, the thickness of the $PbHf_{1-x}Ti_xO_3$ layers is fixed for the chemistry-dependent studies, depolarizing fields (if applicable) would have the same impact on all the multilayer heterostructures irrespective of the chemistry of the constituent $PbHf_{1-x}Ti_xO_3$ layers. As such, a constant value would be observed for the E_T values corresponding to the various multilayer compositions of the studied heterostructures, had there been an effect of depolarizing field at the interfaces. Such evidence reinforces the assertion about the composition and symmetry of the $PbHf_{1-x}Ti_xO_3$ layers, instead of a significant effect from depolarization field, being influential in manipulating the electrical response and hence the E_T values in the studied heterostructures.

Circling back to the discussion about the electromechanical response, from both the current-density- and polarization-electric field response, the threshold field for the large jump in electromechanical response is found to increase gradually with x in the $PbHfO_3/PbHf_{1-x}Ti_xO_3$ multilayers. As such, the best performing composition (i.e., $PbHfO_3/PbHf_{0.6}Ti_{0.4}O_3$) was found in the middle of both extremes, highlighting the importance of an antiferroelectric-ferroelectric composite-like structural (Figure 3a,c) and electrical (Figure 3f) behavior instead of pure antiferroelectric- or ferroelectric-like properties for a low-field onset to the field-induced phase transition for the heterostructures with a high ε. This observation can be corroborated by density-functional-theory (DFT) calculations (Experimental Section) on the $PbHf_{1-x}Ti_xO_3$ system which show that for the mixed-phase-based compositions like $PbHf_{0.6}Ti_{0.4}O_3$, the constituent phases become quasi-degenerate in energy (Note S2, Supporting Information).

2.2. Varying Interface Density in the Nanoscale-Multilayer Heterostructures

As was discussed earlier, strong electromechanical response can be achieved in thin films of antiferroelectrics and here the low-field onset of the large jump in ε (related to the antiferroelectric-to-ferroelectric phase transition) can be tuned with the

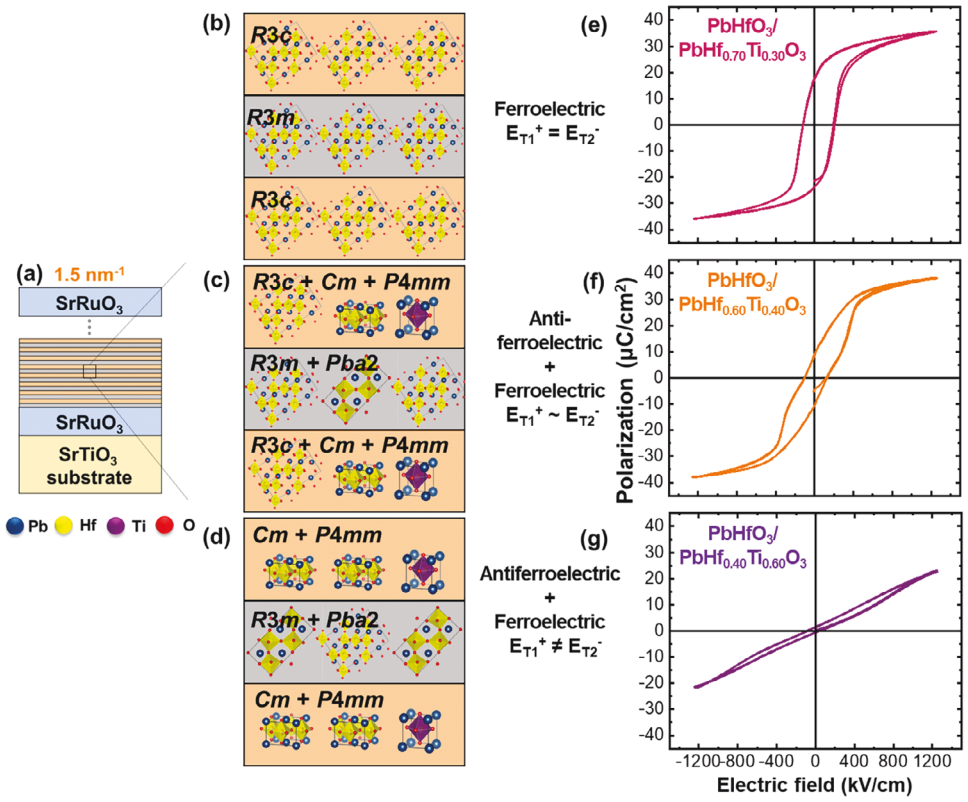

Figure 3. Schematic showing a representation of the multiple crystallographic symmetries of the constituent crystal structures expected in the individual layers and polarization-electric field hysteresis loop for 120-nm-thick b,e) $PbHfO_3/PbHf_{0.7}Ti_{0.3}O_3$, c,f) $PbHfO_3/PbHf_{0.6}Ti_{0.4}O_3$, and d,g) $PbHfO_3/PbHf_{0.4}Ti_{0.6}O_3$ (1.5 nm^{-1}) heterostructures owing to field-induced structural phase transitions.

chemistry of the layers. This is, however, only part of the story with these heterostructures. Tuning the periodicity could also be key in controlling the magnitude of the responses. Thus far, the interface density (i.e., periodicity or layer thickness) has been held constant at 1.5 nm^{-1}, but for the best-performing composition (i.e., $PbHfO_3/PbHf_{0.6}Ti_{0.4}O_3$), five different interface densities (i.e., 0.008, 0.8, 1.5, 2.3, and 3.1 nm^{-1}; **Figure** 4a) were explored (Experimental Section). The interface density was controlled by fixing the overall heterostructure thickness (120 nm) while changing the thickness and number of the constituent layers. As was the case before, all heterostructures were single-crystalline and fully (002_{pc})-oriented and of high quality, as indicated by the multiple satellite peaks in the X-ray diffraction θ-2θ line scans (Figure 4b) and reciprocal space maps (Figure S7, Supporting Information). Additional details on one extreme, the $PbHfO_3/PbHf_{0.6}Ti_{0.4}O_3$ (0.008 nm^{-1}) heterostructures, are also provided (Note S3; Figure S8, Supporting Information). The ε and E_B values are strongly influenced by the interface density. While all multilayers exhibited an enhancement of ε compared to the single-layer films, the range of maximum responses (1.5–4.8%) was primarily dictated by the change in E_B (Figure 4c; wherein heterostructures are driven to an equivalent maximum field value based on their breakdown strength). For example, the $PbHfO_3/PbHf_{0.6}Ti_{0.4}O_3$ (0.008, 0.8, 1.5, and 2.3 nm^{-1}) multilayers exhibited antiferroelectric-like behavior with a significant change in the slope of the strain-field plot at electric-field values close to the antiferroelectric-to-ferroelectric phase transition (i.e., 616, 830, 1215, and 930 kV cm^{-1}, respectively). The $PbHfO_3/PbHf_{0.6}Ti_{0.4}O_3$ (3.1 nm^{-1}) multilayers, however, exhibited ferroelectric-like electromechanical response (i.e., it increases effectively linearly with field). This is thought to be due to the high interface density which makes the overall response of the multilayer heterostructures closer to that of a solid solution instead of retaining the individual material behaviors of the constituent layers. Considering the maximum attainable ε was significantly controlled by the maximum applied field, studying the evolution of E_B is important.

E_B values for the different heterostructures were obtained by measuring the polarization-field response while slowly increasing the maximum applied field for 15 different capacitor structures, from which a Weibull-distribution function was used to extract a statistically meaningful E_B (Experimental Section, Figure 4d). Mirroring the trend in the E_T for the electromechanical switching, a maximum E_B (6.89 ± 0.5 MV cm^{-1}) was obtained for the $PbHfO_3/PbHf_{0.6}Ti_{0.4}O_3$ (1.5 nm^{-1}) multilayers; nearly six- and nine-times that obtained for single-layer $PbHfO_3$ (1.23 MV cm^{-1})[26] and $PbHf_{0.6}Ti_{0.4}O_3$ (0.75 MV cm^{-1}),[27] respectively. Multiple interdependent parameters can affect the E_B of a capacitor, including the leakage-current density, dielectric constant (ϵ_r), defect concentration, bandgap, etc.[39] and a good many of these can be further influenced by the changing interface density. To some extent, because all heterostructures were produced using the same process and starting materials, there is little expectation that many of these items (e.g., defect concentration)

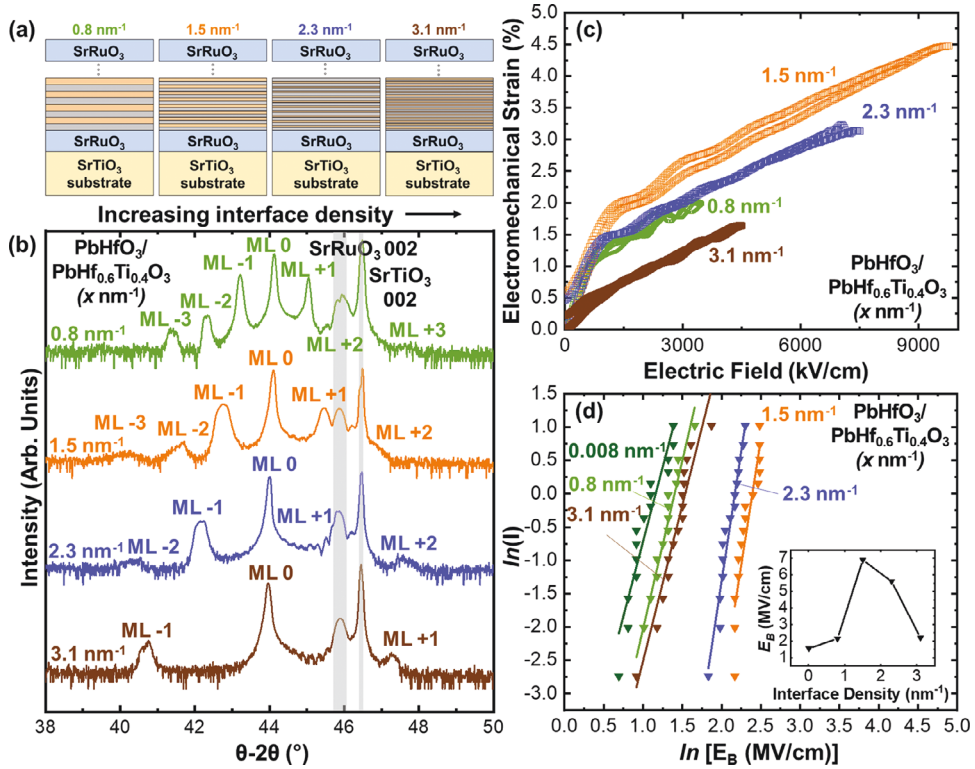

Figure 4. a) Schematic showing the cross-section of the various heterostructures with different interface density values and b) corresponding X-ray-diffraction measurements (θ-2θ line scan) for those heterostructures. For in $PbHfO_3/PbHf_{0.6}Ti_{0.4}O_3$ (0.8, 1.5, 2.3, and 3.1 nm^{-1}) heterostructures, the c) electromechanical strain extracted from the surface displacement loops as a function of electric field (positive bias) at a frequency of 1 kHz, and d) Weibull analysis for determination of E_B where l on the y-axis represents $\ln \frac{1}{1-\frac{i}{16}}$; inset shows the variation in E_B as a function of interface density at 10 kHz and 25-micron diameter capacitors.

will be different. Further, leakage-current-density measurements (Experimental Section) reveal that the 1.5 nm^{-1} heterostructures also have the lowest overall leakage (i.e., are the most electrically insulating), consistent with these same heterostructures exhibiting the highest E_B (Figure S9, Supporting Information). The ϵ_r for the multilayers, on the other hand, was not only lower in magnitude than that for the single-layer parent compositions (Figures S10a–d and S11, Supporting Information) but also was found to decrease systematically with increasing interface density (Figure S10e, Supporting Information), akin to similar studies with other materials.[40–42] Up to an interface density 2.3 nm^{-1}, the lower ϵ_r of the heterostructures as compared to that for the parent compositions could be a governing reason for an enhanced E_B considering the latter is often found to be inversely proportional to $\sqrt{\epsilon_r}$.[43] This does not, however, hold true for the $PbHfO_3/PbHf_{0.6}Ti_{0.4}O_3$ (3.1 nm^{-1}) multilayers which exhibit a lower E_B (2.2 MV cm^{-1}), despite having a ϵ_r value lower than that for the $PbHfO_3/PbHf_{0.6}Ti_{0.4}O_3$ (1.5 and 2.3 nm^{-1}) multilayers. This is likely explained by the prior assertion that the high interface density drives such heterostructures to respond more like a single-layer solid-solution instead of a multilayer. In fact, for the $PbHfO_3/PbHf_{0.6}Ti_{0.4}O_3$ (3.1 nm^{-1}) heterostructures, which have a net composition of $PbHf_{0.8}Ti_{0.2}O_3$, $\epsilon_r \approx 138$ is very similar to that for the single-layer $PbHf_{0.75}Ti_{0.25}O_3$ heterostructures ($\epsilon_r \approx 125$; Figure S10e, Supporting Information).[27] Additionally, DFT calculations (Experimental Section) demonstrated similar trends where increasing the interface densities from 0.5 to 2.5 nm^{-1} could increase the bandgap by 0.35-0.52 eV for the $PbHfO_3/PbHf_{1-x}Ti_xO_3$ heterostructures (Table S2, Supporting Information). Such an observed enhancement of E_B at an optimum interface density is also consistent with past experimental studies wherein $PbZrO_3/PbZr_{0.35}Ti_{0.65}O_3$[40] and $PbZrO_3/Pb_{0.92}La_{0.08}Zr_{0.65}Ti_{0.35}O_3$[44] multilayers exhibited notable improvement in E_B as compared to single-layer heterostructures owing to similar interface effects.[42] Finally, it is contended that the observation of enhancement of properties such as E_B and ϵ at intermediate interfacial-density levels is consistent with the interpretation that more interfaces help reduce the effects of leakage, but there is a limitation set by the thickness wherein the constituent materials transition from being an assembly of individual entities to something more like a solid solution, as seen in past studies.[23,45]

2.3. Validating the Electromechanical Performance and Exploring Its Implications

Finally, considering that the heterostructures are being subjected to both large applied electric fields and ϵ as high as 4.8%, the electrical and mechanical integrity of the best-performing heterostructures (i.e., $PbHfO_3/PbHf_{0.6}Ti_{0.4}O_3$ (1.5 nm^{-1}) multilayers) were investigated using both cycling-based

fatigue/endurance and temperature-dependent dielectric studies (Experimental Section). Heterostructures, when subjected to 2000 kV cm^{-1} applied fields, exhibited only small (<15% degradation) in ε values (2-2.5%) and consistent shape and magnitude of the polarization-electric-field hysteresis loops even after 10^{10} cycles (Figure S12, Supporting Information). Measurements of the dielectric constant and loss as a function of temperature (25-305 °C) revealed a peak at ≈200 °C indicating a transition from the (anti)ferroelectric to a non-polar paraelectric phase, slightly lower in temperature than that same transition observed in single-layer $PbHfO_3$ (255 °C) and $PbHf_{0.6}Ti_{0.4}O_3$ (275 °C) heterostructures (Figure S13, Supporting Information),[26,27] while maintaining a low loss (<0.1) across the entire frequency and temperature ranges studied. These observations point to the robustness of the effects and the absence of strain- and/or field-induced deleterious effects that could limit their use even after being driven to electric fields as high as 6.89 MV cm^{-1} and/or ε values as high as 4.8% with no evidence of mechanical failure (i.e., cracking). Additionally, it is important to note that while the clamping from the geometry of the film on a semi-infinite substrate could provide some added benefit to the response achieved from the antiferroelectric-to-ferroelectric transition in the $PbHfO_3$ layers (as discussed in the Introduction section and ref. [22]), there is no contribution to the measured ε values for the multilayer heterostructures due to substrate bending; consistent with past studies on films in similar geometries (Note S4, Supporting Information). To further assuage concerns regarding any contribution of substrate-induced bending, the origin of the response (especially at high electrical field values) is revisited. First, ε values were measured both under positive and negative applied electric fields and reveal symmetric response (Note S5, Supporting Information); akin to that seen in $PbZrO_3$ films in a similar sample geometry (Figure S14, Supporting Information). Second, once the system has undergone the volume change associated with the antiferroelectric-to-ferroelectric transition (typically done by ≈1500 kV cm^{-1}), the data are linear in nature suggesting that the response is not dominated by electrostriction (which should have a quadratic evolution with field, Note S5, Supporting Information) and further reinforcing the idea that the electromechanical response is primarily piezoelectric in nature.

Having validated the observed electromechanical response, it is valuable to circle back to the rising need for MEMS- and NEMS-based devices necessitating high-performance piezoelectric thin-film heterostructures. While gauging the piezoelectric performance of the synthesized heterostructures in a standardized device configuration as that for a resonator, sensor, actuator, transducer or a "piezotronic" transistor is beyond the scope of this work, it is important to note that all of the aforementioned applications require materials' parameters like high d_{33}, low ϵ_r along with a high E_B and ε.[2–4] The values of d_{33}, ϵ_r, E_B, and, ε are 171 pm V^{-1}, 240, 6.89 MV cm^{-1}, and 4.8%, respectively, for the best performing material in this work are quite promising – a point made clear by comparing with the electromechanical performance of a 100-nm-thick $PbZr_{0.52}Ti_{0.48}O_3$ film (morphotropic phase boundary composition, renowned for its electromechanical response in the bulk). Using the field-dependent ε plots for both cases, two key performance parameters for NEMS-based devices (e.g., piezoelectric micromachined ultrasonic transducers, PMUT)[46] are discussed: deflection sensitivity (representative of d^*_{ij}) and sensing/receiving sensitivity. While a high magnitude for deflection sensitivity is sought for most transducing applications, a low magnitude is desired for sensing/receiving sensitivity.[46] It is important to note that such performance parameters are not typically measured for clamped thin films, but for films in diaphragm- or cantilever-based geometries; nonetheless, they can be used here as a metric to gauge the material's performance. It is evident that the studied heterostructures can demonstrate a higher deflection sensitivity (171 pm V^{-1}) and sensing/receiving sensitivity (5.46 V nm^{-1}) as compared to that for $PbZr_{0.52}Ti_{0.48}O_3$ (43 pm V^{-1} and 29.05 V nm^{-1}, respectively) (Figure S15, Supporting Information) indicating a superior electromechanical performance when implemented as a transducer and comparing to materials in a similar geometry. As such, through appropriate engineering of the interfaces across the studied antiferroelectric-based thin-film heterostructures one can enable the realization of extraordinary ε values accompanied with a superior insulating behavior up to field values as high as 6.89 MV cm^{-1} with a potential of being implemented as an electromechanically-active layer for sensor, actuator, and transducer-based applications for emerging miniaturized technologies.

3. Conclusion

In summary, the potential of antiferroelectric materials as multilayer heterostructures for next-generation electromechanical applications has been demonstrated. Their performance well-surpasses that of traditionally materials while being considerably less affected by substrate-induced clamping. Specifically, multilayer heterostructures based on MPB-based $PbHf_{1-x}Ti_xO_3$ and $PbHfO_3$ manifest extraordinary possibilities in terms of both electrical and electromechanical responses, exhibiting $\varepsilon \approx$ 4.8% with $E_B \approx$ 6.89 MV cm^{-1}. Composition-dependent studies for these $PbHfO_3/PbHf_{1-x}Ti_xO_3$ heterostructures for x = 0.3 and ≥ 0.4 revealed ferroelectric- and antiferroelectric-like behavior, respectively, with the threshold for the antiferroelectric-to-ferroelectric transition increasing with x while exhibiting a high $\varepsilon \approx$ 3–4.8%. Interface-density-dependent studies for $PbHfO_3/PbHf_{0.6}Ti_{0.4}O_3$ (0.008–3.1 nm^{-1}) heterostructures revealed the importance of having an optimum interface density which strongly effects and lowers the ϵ_r and, thereby, results in ultrahigh E_B values in the multilayers that allow one to apply fields that produce colossal $\varepsilon \approx$ 4.8%. Cyclic testing also reveals robust fatigue/endurance behavior of the heterostructures which exhibit <15% degradation in ε values up to 10^{10} cycles without any evidence about induced mechanical failure in the heterostructures. Additionally, if implemented as an active layer in sensor, actuator, or transducer-based applications, the studied heterostructures are expected to demonstrate superior performance as compared to other traditional systems as it pertains to deflection and sensing/receiving sensitivity. Overall, the current work provides a systematic way of realizing and tailoring antiferroelectric materials' behavior in thin-film heterostructures for superior electromechanical response which are robust against substrate clamping and arise from a combination of effects.

4. Experimental Section

Growth of Single-Layer Thin Films: 50–200-nm-thick $PbHfO_3$ and 120-nm-thick $PbHf_{1-x}Ti_xO_3$ (x = 0.3, 0.4, 0.5, and 0.6) thin-film heterostructures were synthesized on 0.5-mm-thick $SrTiO_3$ (001) substrates using pulsed-laser deposition with 45-nm-thick $SrRuO_3$ as both the top and bottom electrodes. Growth was performed by ablating ceramic targets using a KrF excimer laser (248 nm, LPX 300, Coherent), in an on-axis geometry with the target-to-substrate distance as 55 mm. In all cases, the $SrRuO_3$ bottom (top) electrodes were grown at a laser fluence of 1.95 J cm^{-2}, laser repetition rate of 20 Hz, a heater temperature of 700 °C (650 °C), a dynamic oxygen pressure of 100 mTorr, and using ceramic targets with composition $SrRuO_3$. Multiple growth conditions and target chemistries were explored for synthesizing the $PbHfO_3$ and $PbHf_{1-x}Ti_xO_3$ systems. The best results were obtained for $PbHfO_3$ [$PbHf_{1-x}Ti_xO_3$ (x = 0.3, 0.4, 0.5, and 0.6)] heterostructures grown on $SrTiO_3$ (001) substrates at a laser fluence of 1.93 J cm^{-2}, a laser repetition rate of 5 Hz, heater temperature of 600 °C (650 °C), a dynamic oxygen pressure of 100 mTorr, and using ceramic targets with composition $PbHfO_3$ [$Pb_{1.1}Hf_{1-x}Ti_xO_3$ (x = 0.3, 0.4, 0.5, and 0.6)]. For all the growth processes, the heterostructures were cooled from the growth temperature to room temperature at 10 °C min^{-1}. in a static oxygen pressure of ≈760 Torr.

Growth of Multilayer Thin-Film Heterostructures: 120-nm-thick $PbHfO_3/PbHf_{1-x}Ti_xO_3$ (x = 0.3, 0.4, 0.5, and 0.6) multilayer heterostructures were synthesized on 0.5-mm-thick $SrTiO_3$ (001) substrates using pulsed-laser deposition with 45 nm-thick $SrRuO_3$ as the top and bottom electrodes (using the conditions noted above). The multiple interfaces between the two constituent layers $PbHfO_3$ and $PbHf_{1-x}Ti_xO_3$ (x = 0.3, 0.4, 0.5, and 0.6) were created using alternate ablation from two parent targets [i.e., $PbHfO_3$ and $Pb_{1.1}Hf_{1-x}Ti_xO_3$ (x = 0.3, 0.4, 0.5, and 0.6)] using a programmable target rotator (Neocera, LLC) synced with the excimer laser. In this approach, by alternating a fixed number of pulses from the two different targets in the right proportions, any end composition and/or interface density can be obtained. For the composition-dependent studies, the interface density was fixed at 1.5 nm^{-1}, representative of the presence of 180 interfaces or an average layer thickness of 0.66 nm. Further, for one of the compositions (i.e., 120-nm-thick $PbHfO_3/PbHf_{0.6}Ti_{0.4}O_3$ heterostructures) different interface density values (specifically 0.008, 0.8, 1.5, 2.3, and 3.1 nm^{-1}) were synthesized using the same growth conditions and sample geometry as that for the composition-dependent studies. The interface density (i.e., the number of interfaces in the multilayer heterostructure) was controlled by keeping the overall thickness of the heterostructure fixed at 120 nm while changing the individual thicknesses (number of pulses for each layer) of the constituent layers. The two constituent layers were first assembled as a bilayer heterostructure where the overall thickness of the heterostructure was 120 nm with the bottom 60 nm as $PbHfO_3$ and the top 60 nm as $PbHf_{0.6}Ti_{0.4}O_3$ such that the constituent layers should remain as individual entities while being single-crystalline and epitaxial heterostructures in the out-of-plane direction. The bilayer heterostructure contained a single interface between the 60-nm-thick constituent layers, thus the interface density is noted to be 1/120 nm or 0.008 nm^{-1}. Other interface densities were created by alternating growth as appropriate.

Structural Characterization Using X-Ray Diffraction: X-ray diffraction studies were performed on the various $PbHfO_3$ and $PbHf_{1-x}Ti_xO_3$ (x = 0.3, 0.4, 0.5, and 0.6) single-layer films, $PbHfO_3/PbHf_{1-x}Ti_xO_3$ (x = 0.3, 0.4, 0.5, and 0.6; 1.5 nm^{-1}) heterostructures, and $PbHfO_3/PbHf_{0.6}Ti_{0.4}O_3$ (0.008, 0.8, 1.5, 2.3, and 3.1 nm^{-1}) heterostructures with a high-resolution X-ray diffractometer (Panalytical, X'Pert^3 MRD) using a copper source (filtered for just K_α radiation) with 1/2° and 1/16° slits for the incident optics and a 0.275 mm slit for the diffracted-beam optics with the PIXcel3D-Medipix3 detector. The out-of-plane structure of the heterostructures (perpendicular to the plane of the substrate) was probed using θ-2θ line scans. The crystalline quality of the heterostructures in the plane of the substrate was assessed using X-ray rocking curves about the 002_{pc}-diffraction condition of all heterostructures. Further, (a)symmetric azimuthal scans were carried out about the *R3c* $1\bar{1}8_R$-, *Cm* $20\bar{2}_M$-, and *P4mm* 112-diffraction conditions corresponding to the rhombohedral, monoclinic, and tetragonal crystal structures, respectively, for the $PbHf_{1-x}Ti_xO_3$ material system. Additionally, to determine the crystal structure and the lattice parameters for all the synthesized multilayer heterostructures, X-ray diffraction reciprocal space mapping (RSM) studies were performed about the $SrTiO_3$ 103- and 202-diffraction conditions, as required.

Electrical and Dielectric Characterization: All the electrical measurements for $PbHfO_3$ and $PbHf_{1-x}Ti_xO_3$ (x = 0.3, 0.4, 0.5, and 0.6) single-layer films, $PbHfO_3/PbHf_{1-x}Ti_xO_3$ (x = 0.3, 0.4, 0.5, and 0.6) heterostructures with a fixed interface density of 1.5 nm^{-1}, and $PbHfO_3/PbHf_{0.6}Ti_{0.4}O_3$ (0.008, 0.8, 1.5, 2.3, and 3.1 nm^{-1}) heterostructures were conducted inside an acoustic enclosure (isolated with respect to ambient light and noise) with the electric bias being applied to the capacitor heterostructures through the top electrode with the bottom electrode being grounded. The measurements were performed with circular capacitors (diameter 25–50 µm) patterned on the top electrode using photolithography, followed by wet etching of the top $SrRuO_3$ layer using 0.1M $NaIO_4$ solution. The polarization values were measured as a function of electric field (−10000 to 10000 kV cm^{-1}) at room temperature using a Precision Multiferroic Tester (Radiant Technologies, Inc.). Additionally, using the same tester, the leakage current-density measurements were performed for $PbHfO_3/PbHf_{0.6}Ti_{0.4}O_3$ (0.008, 0.8, 1.5, 2.3, and 3.1 nm^{-1}) heterostructures as a function of applied electric field (-2500 to 2500 kV cm^{-1}) at a fixed frequency of 10 kHz, with 100 data points in total for the entire voltage sweep and a soak time of 0.1 s at each data point. Further, for cycling-based fatigue/endurance studies, the heterostructures were excited with a triangular waveform at a maximum electric field value of ±2000 kV cm^{-1} at a frequency of 10 kHz in order to measure the polarization-electric-field hysteresis loops as a function of increasing number of cycle number up to 10^{10} cycles. Dielectric and loss tangent measurements were also performed as a function of frequency (1-100 kHz), DC electric field (−1000 to 1000 kV cm^{-1}), and up to a maximum AC field strength value of 80 kV cm^{-1} using an E4990A Impedance Analyzer (Keysight Technologies). For the frequency-dependent DC bias measurements, an AC signal with an excitation amplitude of 10 mV (0.83 kV cm^{-1}) was applied with the frequency being varied between 1 and 100 kHz for a fixed applied background DC bias. For the temperature-dependent dielectric and loss tangent measurements, an AC signal with an excitation amplitude 10 mV (0.83 kV cm^{-1}) and frequency 10 kHz was applied for the temperature range 25–305 °C.

For the determination of E_B, the polarization response was measured (as described earlier) as a function of electric field for 15 different circular capacitors (diameter 25 µm) for the different $PbHfO_3/PbHf_{1-x}Ti_xO_3$ multilayer heterostructures by driving each of them to the corresponding electrical breakdown. The electrical field for all the measurements was applied at a fixed frequency of 10 kHz. Further, the Weibull distribution was used to provide a reliable estimate of E_B values, in each case. The statistically-relevant E_B values can be determined by performing linear interpolation for the 15 data points for 15 different capacitors in the plot, with $\ln(E_B$ in MV/cm) and $\ln(\ln(\frac{1}{1-\frac{i}{16}}))$ along the x- and y-axis, respectively.

Electromechanical Characterization with Laser Doppler Vibrometry: The capacitor heterostructures were electrically stimulated using a ferroelectric tester (Precision Multiferroic Tester, Radiant Technologies, Inc.) at frequency values 1, 10, and 100 kHz while being simultaneously exposed to a 2-µm-diameter HeNe laser beam (λ = 633 nm) incident on the surface of the 25-µm-diameter top electrode. The vertical electromechanical surface displacement of the capacitor structures along the laser's path was detected using the principle of the Doppler effect. The magnitude of the response was monitored using a laser Doppler vibrometer (PolyTech GmbH) at a sensitivity setting of 5 nm V^{-1}, used in conjunction with the ferroelectric tester. Further, for the cycling-based fatigue/endurance studies, the heterostructures were excited with a triangular waveform at a maximum electric field value of ±2000 kV cm^{-1} at a frequency of 10 kHz in order to measure the electromechanical surface displacement as a function of increasing number of cycles up to 10^{10} cycles. The electromechanical surface displacement value solely due to the layers of interest in the studied heterostructures was obtained by subtracting the contribution due to the electrodes (i.e., $SrRuO_3$) from the overall measured value based on

previously developed methods[12] followed by the calculation of ε (in %) by dividing the obtained surface displacement value by the thickness of the layer of interest. As such, based on the electrical feedback received by the sensors in the ferroelectric tester, the electromechanical surface displacement and ε values were determined as a function of electric field as per the sensitivity of the measurement. In reference to the experimental setup, it is important to note that the heterostructures (i.e., the films on substrates) were adhered first onto a glass slide which was further affixed on a rigid multi-axes stage assembled using a combination of two manual translation platforms meant for controlling the lateral (left-right) and fore-aft motion followed by a dual-tilt platform (Radiant Technologies, Inc.) which limits the scope for substrate-bending-based surface deflection (if any).

First-Principles Calculations: First-principles calculations were performed using the Vienna Ab-initio Simulation Package (VASP),[47] a DFT code employing the projected-augmented wave (PAW) method in combination with plane-wave basis sets. Interface densities from ≈0.5 and up to 2.5 nm^{-1} (assuming a lattice constant of 4.0 Å) were constructed by sequentially stacking $PbHfO_3$ and $PbHf_{1-x}Ti_xO_3$ unit cells with *P4mm* symmetry. Removing the symmetry constraint does not influence the final conclusion. The effect of disorder at the titanium/hafnium sites was modeled using the virtual crystal approximation (VCA) method. The exchange-correlation potential was treated using the meta-GGA r2SCAN[48] functional. To ensure the results were not sensitive to the choice of exchange-correlation functional, the GGA exchange-functionals PBE[49] and PBEsol[50] was also tested without observing any significant changes (Note S2, Supporting Information). The energy cutoff of the plane-wave was set to 600 eV while the *k*-points space was sampled using a gamma-centered grid with a reciprocal density of 200. This corresponds to a 9 × 9 × 4 and a 9 × 9 × 1 grid for the 1/1 and 5/5 heterostructures, respectively. For the calculations of the electromechanical responses and of the phase-stability evolution as a function of the composition, 6 × 4 × 3, 6 × 6 × 2, 6 × 6 × 8, 8 × 8 × 8, and 8 × 8 × 8 k-points grid was used for the *Pbam*, *R3c*, *Cm*, *P4mm*, and *Pm$\bar{3}$m* structures, respectively. All structures were relaxed until all forces on atoms were lower than 0.001 eV $Å^{-1}$. Pymatgen[51] was used to manipulate the input and output files generated by VASP.

Supporting Information

Supporting Information is available from the Wiley Online Library or from the author.

Acknowledgements

This work was primarily supported by the U.S. Department of Energy, Office of Science, Office of Basic Energy Sciences, Materials Sciences and Engineering Division under Contract No. DE-AC02-05-CH11231 (Materials Project program KC23MP) for the discovery of novel functional materials. D.K. acknowledges support from the National Science Foundation under Grant DMR-2102895. H.P. and L.W.M. acknowledge the support of the Air Force Office of Scientific Research under award number FA9550-24-1-0266. Any opinions, findings, and conclusions or recommendations expressed in this material are those of the author(s) and do not necessarily reflect the views of the United States Air Force. B.H., J.E.S., and L.W.M. acknowledge the Army Research Office via Grants W911NF-21-1-0118 and W911NF-21-1-0126 and that this research was sponsored by the Army Research Laboratory and was accomplished under Cooperative Agreement Number W911NF-24-2-0100. The views and conclusions contained in this document are those of the authors and should not be interpreted as representing the official policies, either expressed or implied, of the Army Research Laboratory or the U.S. Government. The U.S. Government is authorized to reproduce and distribute reprints for Government purposes notwithstanding any copyright notation herein.

Conflict of Interest

The authors declare no conflict of interest.

Author Contributions

M.A. and L.W.M. designed the experiments. M.A. synthesized the thin-film heterostructures and performed the structural, electrical, and electromechanical characterization for the same. L.A. and G.H. performed the first-principles calculations. M.A., E.B., L.A., D.K., F.R., H.P., J.N., G.H., and L.W.M. contributed to the analysis and interpretation of the results in the manuscript. M.A. and L.W.M. wrote the core of the manuscript. All authors read the manuscript and contributed to the validation of the message relayed through the same.

Data Availability Statement

Research data are not shared.

Keywords

antiferroelectric, electromechanical strain, ferroelectrics, piezoelectrics, thin films

Received: December 15, 2024
Revised: February 11, 2025
Published online: February 25, 2025

[1] S.-G. Kim, S. Priya, I. Kanno, *MRS Bull.* **2012**, *37*, 1039.
[2] P. Muralt, *Integr. Ferroelectr.* **1997**, *17*, 297.
[3] C. B. Eom, S. Trolier-McKinstry, *MRS Bull.* **2012**, *37*, 1007.
[4] D. L. Polla, L. F. Francis, *MRS Bull.* **1996**, *21*, 59.
[5] S. H. Baek, J. Park, D. M. Kim, V. A. Aksyuk, R. R. Das, S. D. Bu, D. A. Felker, J. Lettieri, V. Vaithyanathan, S. S. N. Bharadwaja, N. Bassiri-Gharb, Y. B. Chen, H. P. Sun, C. M. Folkman, H. W. Jang, D. J. Kreft, S. K. Streiffer, R. Ramesh, X. Q. Pan, S. Trolier-McKinstry, D. G. Schlom, M. S. Rzchowski, R. H. Blick, C. B. Eom, *Science* **2011**, *334*, 958.
[6] R. Keech, S. Shetty, M. A. Kuroda, X. H. Liu, G. J. Martyna, D. M. Newns, S. Trolier-McKinstry, *J. Appl. Phys.* **2014**, *115*, 234106.
[7] M. Copel, M. A. Kuroda, M. S. Gordon, X.-H. Liu, S. S. Mahajan, G. J. Martyna, N. Moumen, C. Armstrong, S. M. Rossnagel, T. M. Shaw, P. M. Solomon, T. N. Theis, J. J. Yurkas, Y. Zhu, D. M. Newns, *Nano Lett.* **2013**, *13*, 4650.
[8] D. M. Newns, B. G. Elmegreen, X. Liu, G. J. Martyna, *Adv. Mater.* **2012**, *24*, 3672.
[9] B. Noheda, D. E. Cox, G. Shirane, J. A. Gonzalo, L. E. Cross, S.-E. Park, *Appl. Phys. Lett.* **1999**, *74*, 2059.
[10] R. Guo, L. E. Cross, S.-E. Park, B. Noheda, D. E. Cox, G. Shirane, *Phys. Rev. Lett.* **2000**, *84*, 5423.
[11] H. Fu, R. E. Cohen, *Nature* **2000**, *403*, 281.
[12] M. Acharya, D. Lou, A. Fernandez, J. Kim, Z. Tian, L. W. Martin, *Phys. Rev. Appl.* **2023**, *20*, 014017.
[13] D. Damjanovic, *J. Am. Ceram. Soc.* **2005**, *88*, 2663.
[14] J. L. Jones, M. Hoffman, J. E. Daniels, A. J. Studer, *Appl. Phys. Lett.* **2006**, *89*, 092901.
[15] Q. M. Zhang, H. Wang, N. Kim, L. E. Cross, *J. Appl. Phys.* **1994**, *75*, 454.
[16] F. Xu, S. Trolier-McKinstry, W. Ren, B. Xu, Z.-L. Xie, K. J. Hemker, *J. Appl. Phys.* **2001**, *89*, 1336.
[17] V. Nagarajan, A. Roytburd, A. Stanishevsky, S. Prasertchoung, T. Zhao, L. Chen, J. Melngailis, O. Auciello, R. Ramesh, *Nat. Mater.* **2003**, *2*, 43.

[18] T. M. Shaw, S. Trolier-McKinstry, P. C. McIntyre, *Mater. Sci.* **2000**, *30*, 263.
[19] H. Liu, H. Wu, K. P. Ong, T. Yang, P. Yang, P. K. Das, X. Chi, Y. Zhang, C. Diao, W. K. A. Wong, E. P. Chew, Y. F. Chen, C. K. I. Tan, A. Rusydi, M. B. H. Breese, D. J. Singh, L.-Q. Chen, S. J. Pennycook, K. Yao, *Science* **2020**, *369*, 292.
[20] M. Waqar, H. Wu, K. P. Ong, H. Liu, C. Li, P. Yang, W. Zang, W. H. Liew, C. Diao, S. Xi, D. J. Singh, Q. He, K. Yao, S. J. Pennycook, J. Wang, *Nat. Commun.* **2022**, *13*, 3922.
[21] Y. Yao, A. Naden, M. Tian, S. Lisenkov, Z. Beller, A. Kumar, J. Kacher, I. Ponomareva, N. Bassiri-Gharb, *Adv. Mater.* **2023**, *35*, 2206541.
[22] H. Pan, M. Zhu, E. Banyas, L. Alaerts, M. Acharya, H. Zhang, J. Kim, X. Chen, X. Huang, M. Xu, I. Harris, Z. Tian, F. Ricci, B. Hanrahan, J. E. Spanier, G. Hautier, J. M. LeBeau, J. B. Neaton, L. W. Martin, *Nat. Mater.* **2024**, *23*, 944.
[23] H. Zhang, N. Pryds, D.-S. Park, N. Gauquelin, S. Santucci, D. V. Christensen, D. Jannis, D. Chezganov, D. A. Rata, A. R. Insinga, I. E. Castelli, J. Verbeeck, I. Lubomirsky, P. Muralt, D. Damjanovic, V. Esposito, *Nature* **2022**, *609*, 695.
[24] M.-M. Yang, Z.-D. Luo, Z. Mi, J. Zhao, S. P. E, M. Alexe, *Nature* **2020**, *584*, 377.
[25] N. D. Sharma, C. M. Landis, P. Sharma, *J. Appl. Phys.* **2010**, *108*, 024304.
[26] M. Acharya, E. Banyas, M. Ramesh, Y. Jiang, A. Fernandez, A. Dasgupta, H. Ling, B. Hanrahan, K. Persson, J. B. Neaton, L. W. Martin, *Adv. Mater.* **2022**, *34*, 2105967.
[27] M. Acharya, H. Ling, D. Lou, M. Ramesh, B. Hanrahan, G. Velarde, M. Asta, K. Persson, L. W. Martin, *Chem. Mater.* **2022**, *34*, 9613.
[28] K. Nadaud, C. Borderon, R. Renoud, M. Bah, S. Ginestar, H. W. Gundel, *J. Alloy Compd.* **2022**, *914*, 165340.
[29] S. E. Reyes-Lillo, K. M. Rabe, *Phys. Rev. B* **2013**, *88*, 180102.
[30] S.-E. Park, M.-J. Pan, K. Markowski, S. Yoshikawa, L. E. Cross, *J. Appl. Phys.* **1997**, *82*, 1798.
[31] K.-Y. Oh, A. Furuta, K. Uchino, *IEEE Sympos. Ultrason.* **1990**, *2*, 743.
[32] C. Bedoya, C. Muller, J.-L. Baudour, F. Bouree, J.-L. Soubeyroux, M. Roubin, *J. Phys. Condens. Matter* **2001**, *13*, 6453.
[33] P. D. Dernier, J. P. Remeika, *Mater. Res. Bull.* **1975**, *10*, 187.
[34] J. Frantti, Y. Fujioka, S. Eriksson, S. Hull, M. Kakihana, *Inorg. Chem.* **2005**, *44*, 9267.
[35] M. F. Kuprianov, S. M. Zaitsev, E. S. Gagarina, E. G. Fesenko, *Phase Transit.* **2006**, *4*, 55.
[36] D. L. Corker, A. M. Glazer, W. Kaminsky, R. W. Whatmore, J. Dec, K. Roleder, *Acta Crystallogr. Sect. B Struct. Sci.* **1998**, *54*, 18.
[37] A. K. Tagantsev, K. Vaideeswaran, S. B. Vakhrushev, A. V. Filimonov, R. G. Burkovsky, A. Shaganov, D. Andronikova, A. I. Rudskoy, A. Q. R. Baron, H. Uchiyama, D. Chernyshov, A. Bosak, Z. Ujma, K. Roleder, A. Majchrowski, J.-H. Ko, N. Setter, *Nat. Commun.* **2013**, *4*, 2229.
[38] H. Liu, L. Fan, S. Sun, K. Lin, Y. Ren, X. Tan, X. Xing, J. Chen, *Acta Mater.* **2020**, *184*, 41.
[39] H. Palneedi, M. Peddigari, G. Hwang, D. Jeong, J. Ryu, *Adv. Funct. Mater.* **2018**, *28*, 1803665.
[40] J. Zhang, Y. Zhang, Q. Chen, X. Chen, G. Wang, X. Dong, J. Yang, W. Bai, X. Tang, *Nanomaterials* **2021**, *11*, 2141.
[41] K. Boldyreva, L. Pintilie, A. Lotnyk, I. B. Misirlioglu, M. Alexe, D. Hesse, *Appl. Phys. Lett.* **2007**, *91*, 122915.
[42] Z. Sun, C. Ma, M. Liu, J. Cui, L. Lu, J. Lu, X. Lou, L. Jin, H. Wang, C. Jia, *Adv. Mater.* **2017**, *29*, 1604427.
[43] J. R. Laghari, W. J. Sarjeant, *IEEE Trans. Power Electron.* **1992**, *7*, 251.
[44] B. Sun, M. Guo, M. Wu, Z. Ma, W. Gao, H. Sun, X. Lou, *Ceram. Int.* **2019**, *45*, 20046.
[45] J. Ravichandran, A. K. Yadav, R. Cheaito, P. B. Rossen, A. Soukiassian, S. J. Suresha, J. C. Duda, B. M. Foley, C.-H. Lee, Y. Zhu, A. W. Lichtenberger, J. E. Moore, D. A. Muller, D. G. Schlom, P. E. Hopkins, A. Majumdar, R. Ramesh, M. A. Zurbuchen, *Nat. Mater.* **2014**, *13*, 168.
[46] K. Roy, J. E.-Y. Lee, C. Lee, *Microsyst. Nanoeng.* **2023**, *9*, 95.
[47] G. Kresse, D. Joubert, *Phys. Rev. B* **1998**, *59*, 1758.
[48] J. W. Furness, A. D. Kaplan, J. Ning, J. P. Perdew, J. Sun, *J. Phys. Chem. Lett.* **2020**, *11*, 8208.
[49] J. P. Perdew, K. Burke, M. Ernzerhof, *Phys. Rev. Lett.* **1996**, *77*, 3865.
[50] J. P. Perdew, A. Ruzsinszky, G. I. Csonka, O. A. Vydrov, G. E. Scuseria, L. A. Constantin, X. Zhou, K. Burke, *Phys. Rev. Lett.* **2008**, *100*, 136406.
[51] S. P. Ong, W. D. Richards, A. Jain, G. Hautier, M. Kocher, S. Cholia, D. Gunter, V. L. Chevrier, K. A. Persson, G. Ceder, *Comput. Mater. Sci.* **2013**, *68*, 314.